Cyclotron-resonance studies of electronic properties in ZnSe

T. Ohyama, K. Sakakibara, and E. Otsuka

Department of Physics, College of General Education, Osaka University, Toyonaka, Osaka 560, Japan

M. Isshiki and K. Igaki

Department of Materials Science, Faculty of Engineering, Tohoku University, Sendai 980, Japan

(Received 23 October 1987)

A cyclotron-resonance experiment has been performed on various ZnSe crystals with different heat treatments, as a function of magnetic field orientation, temperature, and delay time after photopulse excitation. Two-dimensional (2D) characters of the absorption signal consistently show up for a few samples. X-ray analysis and microscopic observation with polarizers reveal a multimosaic structure of numerous twin-crystal boundaries for these samples. These boundaries evidently lead to a formation of potential wells that are responsible for the 2D character. An experiment with a sample free from boundaries enables us to make a precise determination of the effective-mass value and the temperature dependence of the scattering rate of photoexcited electrons. An extra resonance peak is observed in the experiment with a far-infrared laser. It is interpreted as a polaron-induced nonparabolicity effect of the conduction band in ZnSe. In addition, clear evidence of a two-to three-dimensional transition has been observed.

I. INTRODUCTION

Characterization of the electronic properties of ZnSe has always suffered from the fact that even an undoped ZnSe crystal contains many native defects and residual impurities which act as donors.[1,2] Accordingly, though ZnSe is expected to be one of the most promising II-VI materials for fabrication of an efficient blue-light-emitting device, there is as yet no well-established technique to make such devices. Past works on ZnSe were maily concerned with photoluminescence[3-7] and dc transport measurements.[8,9]

Owing to success in making large single crystals of high-quality ZnSe, we initiated an investigation of the carrier transport as well as the dynamical properties of this material through magnetooptical-absorption measurements. Application of an external magnetic field and the photoexcitation technique, which induces a change of the electronic states and the carrier density, are a great help in material characterization, and thus our knowledge of the electronic system in ZnSe should be greatly enhanced by the use of magnetooptics. Millimeter and submillimeter wave magnetoabsorption, which leads the way to study of the band structure, carrier transport, kinetics, etc., has indeed been used to make a direct characterization of such materials as Si, Ge, InSb, and GaAs.[10-13] No comparable experiment, however, exists for ZnSe, except for our preliminary reports.[14-16]

This paper is organized as follows. In Sec. II we present a brief description of our experimental procedures and sample characteristics. In Sec. III an outline of experimental results is described. We finally discuss in Sec. IV some of our findings and present in Sec. V our conclusions as well as suggestions for further studies.

II. SAMPLES AND EXPERIMENTAL PROCEDURES

Several n-type ZnSe crystals have been used in the present experiment. All the crystals were grown by vapor-phase transport using a Zn reservoir.[6] This growth method is the so-called modified Prior method. The characteristics of the material strongly depend on the growth method, kind of dopant, and heat-treatment process.

Sample pieces were cut or cleaved from an as-grown single crystal or some ingots after heat treatment. They were all nearly rectangular- or oval-shaped plates with maximum dimensions of $4 \times 3 \times 1$ mm^3. Samples were mechanically polished with emery paper no. 3000 and chemically etched in a solution consisting of three parts $K_2Cr_2O_7$ and two parts concentrated H_2SO_4 at 90 °C for two minutes, then in CS_2 at room temperature, to remove the deposited selenium layer.

Characteristics of all the samples are summarized in Table I. From photoluminescence experiments it is clarified that the density of zinc vacancies, the acceptors, diminishes to a large extent after "zinc-dip" treatment.[6]

TABLE I. Sample characteristics.

Sample	Treatment
1	as-grown
2	selenium saturation
3	as-grown
4	twin-crystal boundaries taken away from sample 3
5	zinc-dip

Consequently, the electron density of the sample increases appreciably. After the treatment in a saturated selenium vapor, on the other hand, the density of zinc vacancies increases, while that of selenium vacancies, the donors, decreases, thus making the material, in effect, compensated.

In order to seize detailed characteristics of samples, we have tried x-ray analysis and microscopic observation with optical polarizers. Microscopic photographs of samples 3 and 5 are shown in Fig. 1. We can see a clear multimosaic structure in both samples. Through x-ray analysis it is revealed that the structure consists of twin-crystal boundaries which intersect at right angles with the crystal growth direction, $\langle 111 \rangle$. The crystallographic directions are indicated by arrows. Stacking faults as constructed by sheets of twin-crystal boundaries can, as we shall see later on, sometimes accommodate a two-dimensional electronic system.

For the far-infrared (FIR) source, a wavelength of 220 μm (1364 GHz) is obtained from a discharge-type H_2O laser, while wavelengths of 433 μm (692 GHz) and 513 μm (585 GHz) are obtained from a CO_2-laser-pumped cavity. They are operated in pulses at a repetition rate of 30 Hz, if needed, in synchronized combination with the photoexcitation light pulses at 15 Hz. The excitation

Sample 3

$\langle 1\,1\,1 \rangle \longrightarrow$
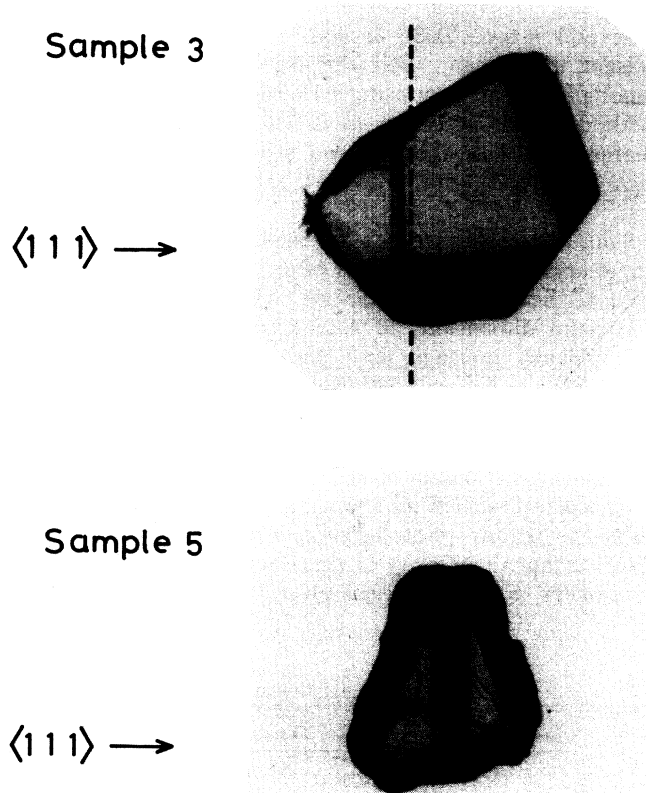
Sample 5

$\langle 1\,1\,1 \rangle \longrightarrow$

FIG. 1. Microscopic photograph of samples 3 and 5 taken with a couple of optical polarizers. Distinct multimosaic structures are visible in both samples. Arrows show the relevant crystallographic axes. The dashed line parallel to "stripes" shows a cutting line. The larger part without "stripes" is designated as sample 4.

light is provided by a xenon flash lamp with a pulse width of 1 μs. The transmitted FIR laser beam is detected by an n-type InSb Putley detector.

The absorption spectra are obtained as $\ln(I_0/I_L)$ by a two-channel boxcar averager with an aperture of 0.5 μs. Here I_L and I_0 are the transmitted beam intensities of the pulsed FIR laser with and without photoexcitation. In the event of an experiment without optical excitation, I_L should be taken as the transmitted laser-beam intensity, I_0 being kept constant.

The microwave setup is a nonresonant reflection-type wave-guide system working at 35 GHz. Temperature is varied between 4.2 and 70 K for both microwave and FIR experiments. A heater on the microwave wave guide or one on the brass-tube transmitting the FIR beam is used to raise the temperature of the sample to a desired level above 4.2 K. The temperature is measured with a calibrated carbon-glass sensor pressed onto the sample holder and controlled with a temperature controller (Oxford Instruments model no. DTC-2).

The FIR experiment is carried out in the Faraday configuration, and a magnetic field up to 10 T is applied along the $\langle 1\bar{1}0 \rangle$ crystallographic axis. In the microwave experiment, the magnetic field is rotated around the $\langle 1\bar{1}0 \rangle$ crystal axis and it has been possible to arrange the angle between the external magnetic field and twin-crystal boundaries at will. Other details are described elsewhere.[17]

III. EXPERIMENTAL RESULTS

A. Far-infrared measurements

Samples used in the FIR experiment are 1, 3, and 5. Experimental results for sample 5 will be touched upon separately.

Figure 2 shows the typical spectra from sample 3 observed at 4.2 K for the wavelength of 220 μm. Observed sharp lines correspond to the cyclotron-resonance absorption by photoexcited carriers taken right after the excitation pulse. Two absorption lines are seen close to each other. They are very similar to those previously observed in sample 1.[14] The main absorption C_1 is the cyclotron resonance of electrons, which yields an apparent effective mass of $m^* = 0.145m_0$. Combined with the measurements at 172 and 433 μm, the electron effective band mass m_b^* has been accurately determined as $(0.134 \pm 0.002)m_0$.[14]

Two possibilities exist as to the origin of the second peak C_2: one is the light-hole signal and the other is a quantum line of the electron owing to the nonparabolic energy band via the polaron effect.[18] Figures 3 and 4 show the temperature dependence of the cyclotron-resonance absorption from sample 5 "without" photoexcitation for wavelengths of 220 and 433 μm, respectively. The magnetic field is applied along the $\langle 1\bar{1}0 \rangle$ crystal axis at a wavelength of 220 μm, which is perpendicular to the flat sample plane. The magnetic field for the wavelength of 433 μm, on the other hand, is applied along the $\langle 111 \rangle$ crystal axis, which is perpendicular to the twin-crystal boundary plane. It should again be emphasized that the
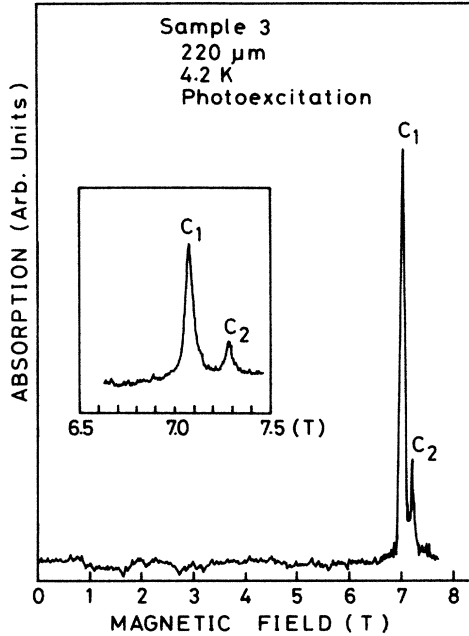
FIG. 2. Far-infrared (220-μm) cyclotron-resonance absorption for sample 3, taken at 4.2 K right after the excitation pulse. The inset shows the same trace with an enlarged abscissa. Two adjacent peaks are clearly observed.

FIG. 3. Cyclotron-resonance traces for sample 5 at various temperatures for the wavelength of 220 μm. Data are taken without photoexcitation. The ground level for each trace is shifted and the recorder gain is changed by a factor of 2.5 between the 29- and 31-K traces. On top of C_1 the secondary resonance C_2 appears as temperature is raised.

above-mentioned signals are observed even without photoexcitation. As will be recognized subsequently through microwave experiments, a dense array of stacking faults as constructed by a sheet of twin-crystal boundaries are building up "stripes" of potential wells into which electrons can be accommodated to form a two-dimensional system even without photoexcitation in sample 5. It can be seen in Fig. 3 that only a single peak is observed at low temperature. A secondary resonance peak, the resonance position of which completely coincides with the signal in samples 1 and 3, appears only as the temperature is raised. Consequently, the second peak commonly observed in samples 1, 3, and 5 for the 220-μm experiment is outside the realm of possibility of a light-hole signal, since holes should not show up in the unilluminated n-type sample 5.

We will then discuss the sole remaining possibility, the polaron effect. In a polar semiconductor such as ZnSe, the interaction of carriers with polar-optical phonons has outstanding effects on energy dispersion as well as on the scattering rate of carriers. The energy spectrum of a polaron in a magnetic field can be calculated in two ways. Bajaj has calculated the transition energy between Landau levels using Onsager's approach, which is useful in the low-magnetic-field case.[19] Another approach has been made by Laresen with Wigner-Brillouin perturbation theory, which is useful near the level crossing where the Landau-level energy overtakes the optical-phonon energy.[18] Larsen gives an algebraic expression only for the first two Landau levels as a function of magnetic field. In order to discuss the secondary resonance position, we need the expression for higher Landau levels. Recently,
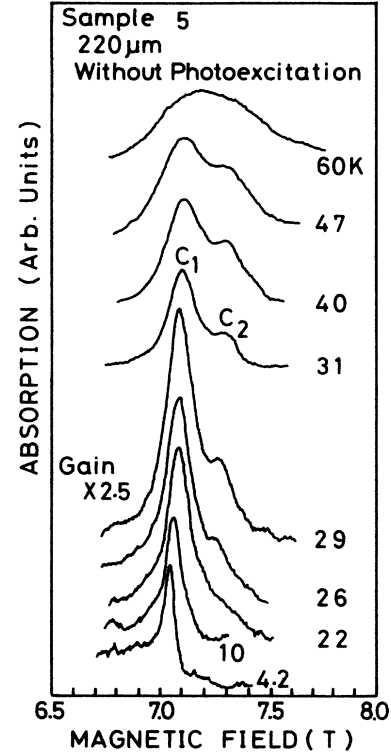
Peeters and Devreese have obtained an expression applicable for all Landau levels, using a second-order perturbation theory.[20] According to their calculation, the electron-phonon contribution to the energy splitting between two successive Landau levels is given by

$$\Delta E_{N+1} - \Delta E_N = -\frac{\alpha\omega_c}{6}\left[1 + \frac{9(N+1)}{10}\omega_c \right.$$
$$\left. + \frac{135N(N+2)+94}{168}\omega_c^2 + \cdots \right],$$

(1)

where $\omega_c = eB/m_b^*$ with the electron band mass m_b^* and the polaron coupling constant α. $\Delta E_N/\hbar$ and ω_c are in units of a LO-phonon frequency ω_{LO}. The cyclotron energy,

$$\hbar\omega_c^*(N+1, N) = E_{N+1} - E_N ,$$

(2)

defines a cyclotron mass

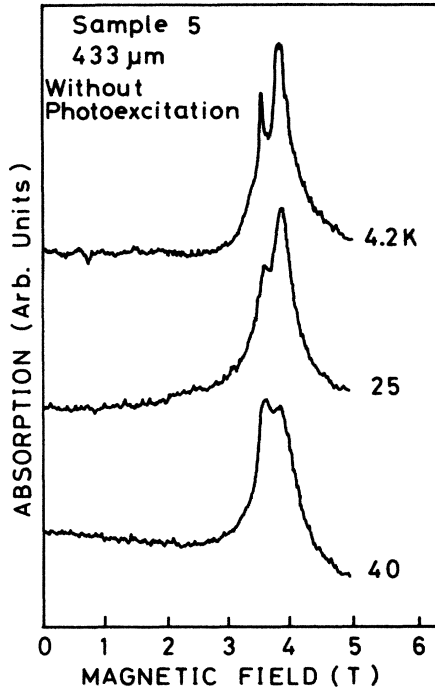$$m^*(N+1, N)/m_b^* = \omega_c/\omega_c^*(N+1, N) ,$$

FIG. 4. Far-infrared (433-μm) cyclotron-resonance traces for sample 5 at various temperatures. Data are taken without photoexcitation.

which is given by

$$\frac{m^*(N+1, N)}{m_b^*} = \frac{1}{1 - \frac{\alpha}{6}\left[1 + \frac{9(N+1)}{10}\omega_c + \cdots\right]} . \quad (3)$$

For the lowest two transitions, we obtain the following mass ratio to the first order of ω_c:

$$\frac{m^*(2,1)}{m^*(1,0)} \approx 1 + \frac{3\alpha\omega_c}{20} . \quad (4)$$

Using the numerical values appropriate to ZnSe, namely $\alpha = 0.432$ (Ref. 21) and $\omega_{LO} = 4.6 \times 10^{13}$ s^{-1},[22] we obtain $m^*(2,1)/m^*(1,0) \simeq 1.012$ for the 220-μm experiment. For the present case $m^*(2,1)$ predicted from the above relation is $0.147m_0$. This value gives fairly good agreement with our experimental results of $0.149m_0$. Conversely, by use of our experimental results and Eqs. (3) and (4), we can derive such α and m_b^* as $\alpha = 0.575$ and $m_b^* = 0.131m_0$.

The intensity ratio $\delta = S_{21}/S_{10}$ is connected with the definition of the so-called electron temperature T_E; strictly speaking, the inter-Landau-level temperature T_{01} which characterizes the electron distribution over the $N = 0$ and 1 levels. Here S_{10} and S_{21} represent the intensities of the lowest two transitions. If the system is in thermal equilibrium, T_E should be equal to the lattice temperature T_L. Generally, the intensity $S_{N+1,N}$ is expressed as

$$S_{N+1,N} = \eta(N+1)(n_N - n_{N+1}) , \quad (5)$$

where n_N is the electron population in the Nth level and η a numerical factor. By writing

$$\frac{n_1}{n_0} = \exp\left[-\frac{\Delta E_{10}}{k_B T_L}\right] , \quad (6)$$

we may write the temperature-versus-population relation in the form

$$\frac{\Delta E_{10}}{k_B T_L} = -\ln\left[\frac{\delta}{2+\delta}\left[1 + \frac{2n_2}{n_0\delta}\right]\right] , \quad (7)$$

where ΔE_{10} is the energy difference between the $N = 0$ and 1 Landau levels. For the 220-μm resonance, we have observed no perceptible signals from conduction electrons populated in Landau levels higher than $N = 2$, so that we may assume $2n_2/n_0\delta \ll 1$ in Eq. (7). Figure 5 shows the electron population ratio n_1/n_0 obtained from experimental data as a function of the reciprocal-lattice temperature. The solid line, on the other hand, gives $\Delta E_{10}/k_B$ with an energy difference of 5.6 meV for the 220-μm experiment. The agreement between the measured and calculated values of the slope provides strong evidence of the validity of our argument. The electron temperature defined by Eq. (6) can readily be derived from our experimental result for sample 3 with photoexcitation. One finds that the electron temperature initially rises as high as 32 K. This electron temperature is derived with help of Fig. 5, using the experimental observation of $\delta = 0.19$ right after the photopulse. Evidently, the lattice temperature remains low, since little line broadening is observed. Such optical hot electrons are observed in InSb.[12] The situation, however, is a little different from the present case. For InSb, strictly speaking, it can
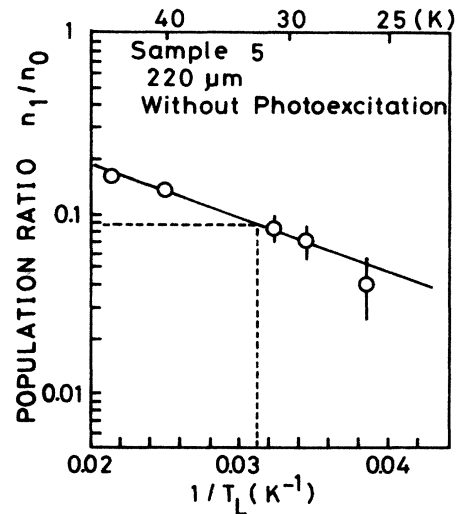

FIG. 5. Fraction of electron density in the $N = 1$ Landau level relative to that in the $N = 0$ Landau level plotted vs the reciprocal temperature. The solid straight line drawn through data points corresponds to the Landau-level separation $\Delta E_{10} = 5.6$ meV according to Eq. (6). The dashed line indicates the procedure determining the electron temperature for the photoexcited system.

be regarded as the spin temperature of the conduction electrons. For ZnSe, on the other hand, it simply corresponds to the inter-Landau-level electron temperature, or the orbital temperature of conduction electrons. At all events, detailed discussions as for optical hot electrons would be worth making in a future extended study.

B. Microwave measurements

Typical traces of cyclotron resonance at 4.2 K with photoexcitation are shown in Fig. 6 for sample 3 at various angles between the magnetic field and a characteristic direction of the crystal. The electron-cyclotron-resonance peak observed at $B = 0.2$ T and 2 μs after the excitation pulse lies on a broad plateau. The absorption signal thus seems to consist of two different kinds of carriers. For the magnetic field direction denoted 0°, we obtain the strongest resonance signal. The intensity of the resonance peak gradually decreases as the magnetic field is rotated; nevertheless, the resonance field is unchanged. When the magnetic field is applied along a certain characteristic direction denoted 90°, the resonance-peak height becomes a minimum and the broad plateaulike absorption becomes dominant. The behavior is more or less the same as the results for sample 1. Figure 7 shows the time-resolved cyclotron-resonance absorption for sample 3 at 4.2 K and with photoexcitation. The excitation spot is centered at the limpid portion (off-boundary "stripes") of the sample. The electron-cyclotron-resonance peak is clearly observed for a few microseconds after the photopulse. The plateau, on the other hand, abruptly increases
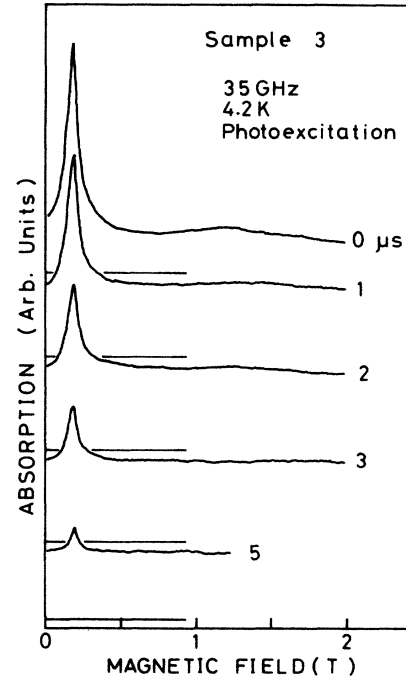
FIG. 7. The delay-time dependence of the cyclotron-resonance signal in sample 3 and at 4.2 K. Delay times t_d, in time resolution after excitation photopulse, are shown on the right. The baseline for each trace is shown on the ordinate. Shortly after a photopulse, the electron-cyclotron-resonance peak on the broad nonresonant absorption is strong and broadened. The nonresonant absorption decreases gradually, passing the maximum at 3 μs after the photoexcitation. One can see a swelling due to the heavy-hole signal near 1.3 T in the 0-μs trace.

after the photoexcitation, reaches the maximum, and decreases gradually. A small swelling at $B = 1.3$ T, which is seen at $t_d = 0$, originates in the heavy-hole cyclotron resonance.[16] Figure 8 shows typical traces of sample 3 at 20 K and with photoexcitation. At this temperature the plateau turns into a secondary resonance peak of which the resonance field is critically dependent on the magnetic field direction.

Figure 9 shows the angular dependence of the resonance field obtained from sample 3 and at 20 K. The solid circles show the data for the resonance peak which appears above 15 K, and the open circles correspond to the resonance peak at $B = 0.2$ T. Judging from above-mentioned experimental results, it certainly seems awkward to bring such a concept as two dimensionality coexisting with three dimensionality into the properties of sample 3. But the two-dimensional (2D) nature is confirmed by the fact that the resonance field is found to shift, corresponding to an isotropic effective mass multiplied by $1/\cos\theta$, where θ is the angle between the applied magnetic field and a characteristic axis of the crystal, that is, the crystal-growth direction, $\langle 111 \rangle$, and coincidentally the perpendicular direction to twin-crystal boundaries.

Cyclotron-resonance traces from sample 5 are shown in Fig. 10 for different orientations of the magnetic field
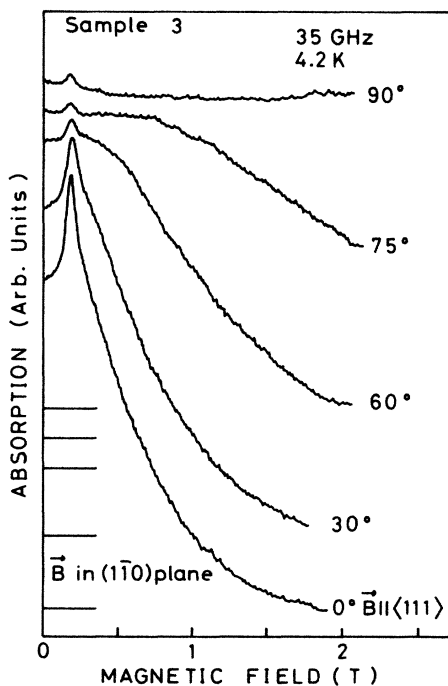

FIG. 6. Microwave cyclotron-resonance traces for samples 3 and for different angles between the magnetic field direction and a characteristic crystal axis. Each trace was taken 2 μs after the photopulse. The baseline for each trace is shown on the ordinate.
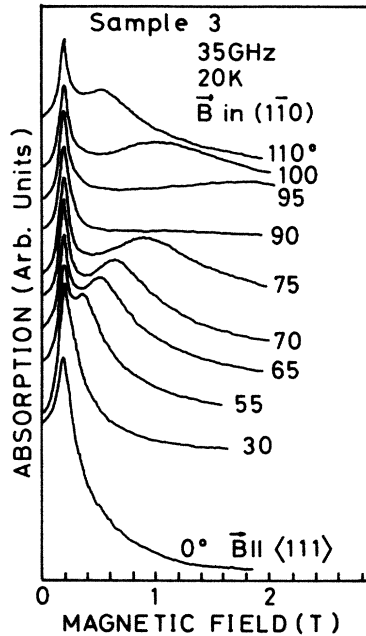
FIG. 8. Traces of the cyclotron-resonance absorption at 20 K from sample 3 are shown at different angles between the magnetic field and a characteristic direction of the crystal, $\langle 111 \rangle$. Angles are shown on the right.
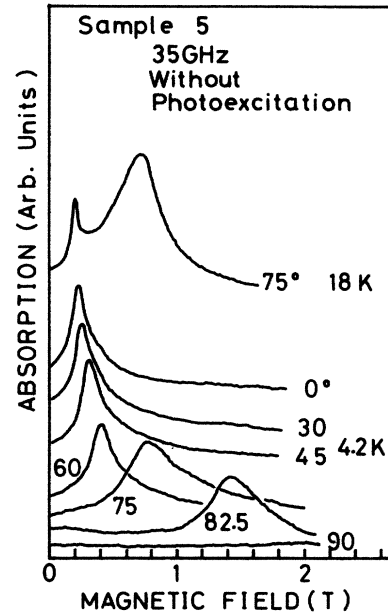

FIG. 10. Microwave cyclotron-resonance signals at 4.2 K from sample 5 for various angles between the magnetic field direction and a characteristic crystal axis $\langle 111 \rangle$. Angles are shown on the right. The data are taken without photoexcitation. Only the trace on the top is taken at 18 K.

relative to a characteristic axis which is analogous to the case of sample 3. Data are taken at 4.2 K and without photoexcitation. At this temperature we observe only a single resonance line, the resonance field of which is again sensitive to the magnetic field direction. The angular dependence of the resonance field shows the same behav-

FIG. 9. The angular dependence of the resonance field: solid circles show the data for 2D electrons and open circles the data for 3D electrons. The data have been taken at 20 K and from sample 3. The dashed line shows a characteristic behavior of $1/\cos\theta$ for 2D electrons, where θ is the angle between the magnetic field and the $\langle 111 \rangle$ direction.

ior as that of sample 3. According to the experimental evidence both for samples 3 and 5, we can conclude that the resonance absorption at $B = 0.2$ T, which is observed only right after the photopulse for sample 3, and only at higher temperatures for sample 5 without photoexcitation, originates in the 3D electrons, while the anisotropic one comes from the 2D electrons confined in the twin-crystal boundaries.

Traces of the cyclotron-resonance absorption by sample 5 for a fixed direction of the magnetic field are shown in Fig. 11 at various temperatures. In addition to the anisotropic resonance peak, an isotropic resonance appears at $B = 0.2$ T as the temperature is raised, and its absorption intensity markedly increases above 20 K.

In order to get proper characteristics of the limpid portion, i.e., the bulk of ZnSe, we have cut sample 3 into two parts along a line parallel to the stripes, which is shown in Fig. 1. We designate a larger part without twin-crystal boundaries as sample 4. For sample 4 it is found that the broad plateau completely disappears and only the isotropic electron signal is observed for the whole temperature range investigated. These facts reveal that the anisotropic character of samples 3 and 5 is due to 2D electrons confined in potential wells of twin-crystal boundaries.

C. Temperature dependence of the resonance linewidth

Traces of the cyclotron-resonance absorption for sample 4 are shown in Fig. 12 at various temperatures and at a fixed delay time of 4 μs. It can be seen that the linewidth steadily increases with temperature. In particular, it broadens rapidly as the temperature is raised above 30 K and the absorption intensity markedly in-
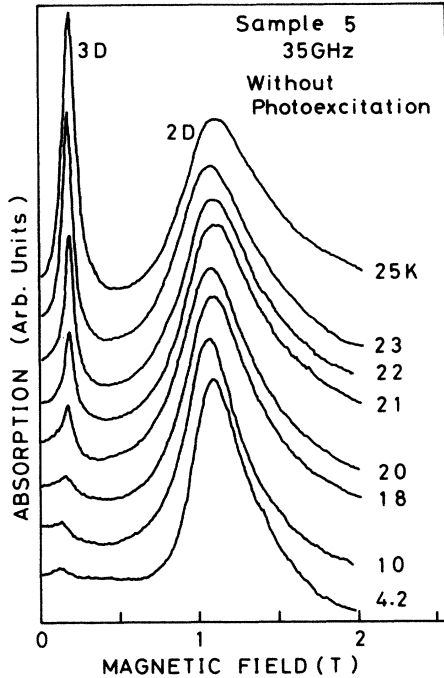
FIG. 11. Cyclotron-resonance traces at various temperatures and at a fixed angle (80°) obtained from sample 5. The data are taken without photoexcitation. A large growth of 3D electrons at high temperatures is quite obvious.
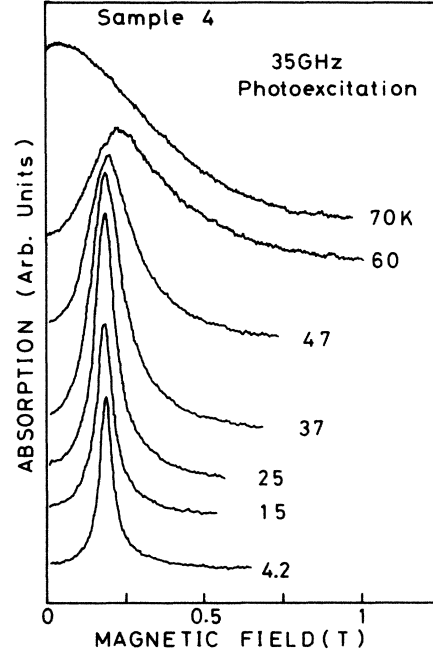

FIG. 12. Cyclotron-resonance traces at various temperatures obtained from sample 4. Line broadening and peak shift at high temperatures, especially above 50 K, are quite obvious.

creases. One may note that, in addition to the line broadening, the peak position at first shifts toward the high magnetic field. Above 60 K the peaking nature of the absorption curve is lost very rapidly. At 65 and 70 K the entire signal is practically of Drude type.

To a good approximation one can get the carrier relaxation time τ through the resonance-linewidth analysis. By a simple relation one can convert the resonance linewidth into the carrier relaxation time τ, i.e., by

$$\frac{1}{\tau} = \frac{\omega \, \Delta B}{B_r} , \tag{8}$$

where ΔB is the half-width, B_r the resonance field, and ω the angular frequency of the source. The temperature dependence of the inverse relaxation time $1/\tau$ is shown in Fig. 13 on a logarithmic scale. The inverse relaxation time is nearly independent of temperature below 10 K, but abruptly increases above 30 K. The behavior is well understood if we interpret the linewidth to be the sum of lattice and neutral-impurity scatterings. We can neglect the contribution of the scattering by ionized impurities. If we shed intrinsic light on the sample and produce electrons and holes, these free carriers are promptly captured by ionized impurities which are thereby neutralized. At low temperatures, the contribution from neutral-impurity scattering flattens the temperature dependence of $1/\tau$.

The electron-scattering rate by neutral donors is well accounted for by the Erginsoy formula,[23]

$$\frac{1}{\tau_{\mathrm{ND}}} = \frac{20 \hbar a_B^* N_D}{m^*} , \tag{9}$$

where a_B^* is the effective Bohr radius of the donor and N_D the donor concentration. Substituting the numerical values appropriate to ZnSe, namely $a_B^* = 33$ Å and $m^* = 0.145 m_0$, one obtains

$$\frac{1}{\tau_{\mathrm{ND}}} = 5.3 \times 10^{-5} N_D \ \mathrm{s}^{-1} , \tag{10}$$
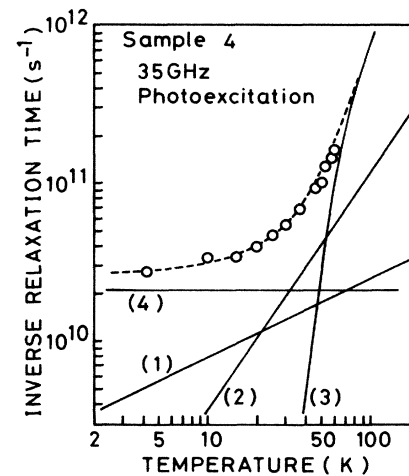

FIG. 13. Temperature dependence of the inverse relaxation time for sample 4. A dashed line shows a theoretical prediction comprising neutral-impurity- and phonon-type scatterings. Phonon-type scatterings comprise (1) acoustic piezoelectric scattering, (2) acoustic deformation-potential scattering, and (3) polar-optical-phonon scattering. Contributions from neutral impurities, (4), have been estimated from low-temperature experimental data.

where N_D is in cm^{-3}.

At higher temperatures, the polar-optical-phonon scattering becomes the most dominant scattering mechanism. The well-known form of the polar-optical-phonon scattering[24] is

$$\frac{1}{\tau_{PO}} = \frac{2\alpha\omega_{LO}}{\exp\left[\dfrac{\hbar\omega_{LO}}{k_B T_L}\right] - 1} . \tag{11}$$

With $\alpha = 0.432$ and $\hbar\omega_{LO}/k_B = 360$ K (Ref. 22) for ZnSe, one obtains

$$\frac{1}{\tau_{PO}} = \frac{4.0 \times 10^{13}}{\exp\left[\dfrac{360}{T_L}\right] - 1} \text{ s}^{-1} , \tag{12}$$

where T_L is in K. In the intermediate-temperature range there are two other phonon-scattering mechanisms which influence the temperature dependence of $1/\tau$, i.e., acoustic–deformation-potential[25] and acoustic-piezo-electric[26] scatterings. They are approximated by

$$\frac{1}{\tau_{DP}} = \frac{3m^{*\,3/2}C_1^2(k_B T_L)^{3/2}}{(8\pi)^{1/2}\hbar^4\rho c_s^2} \tag{13}$$

and

$$\frac{1}{\tau_{pz}} = \frac{e^2 m^{*\,1/2}(k_B T_L)^{1/2}K^2}{16(2\pi)^{1/2}\hbar^2\epsilon_s} , \tag{14}$$

respectively. Here C_1 is the deformation-potential constant, ρ the density of crystal, c_s the longitudinal sound velocity, K the piezoelectric coupling constant, and ϵ_s the static dielectric constant. Expressed in a numerical style, Eqs. (13) and (14) yield

$$\frac{1}{\tau_{DP}} = 5.7 \times 10^7 T_L^{3/2} \text{ s}^{-1} \tag{15}$$

and

$$\frac{1}{\tau_{pz}} = 5.9 \times 10^9 T_L^{1/2} \text{ s}^{-1} , \tag{16}$$

respectively, where T_L again is in K. In deriving Eqs. (15) and (16), we employ the following numerical values: $\rho c_s^2 = 1.1 \times 10^{12}$ dyn cm^{-2},[8] $C_1 = 4$ eV,[8] $K = 0.0437$,[27] and $\epsilon_s = 8.1$.[8] The comparison between our experiment and theoretical calculation is shown in Fig. 13. Experimental data essentially agree with theoretical prediction if we take $N_D = 4.0 \times 10^{14}$ cm^{-3}.

D. Temperature dependence of polaron mass

The temperature dependence of the electron mass derived from the resonance-peak position is shown in Fig. 14. This mass shift is thought to arise from the nonparabolicity of the conduction band by the polaron effect enhanced in a polar semiconductor such as ZnSe. As the temperature is increased, more and more electrons populate higher Landau levels and give rise to resonance lines at higher magnetic fields.
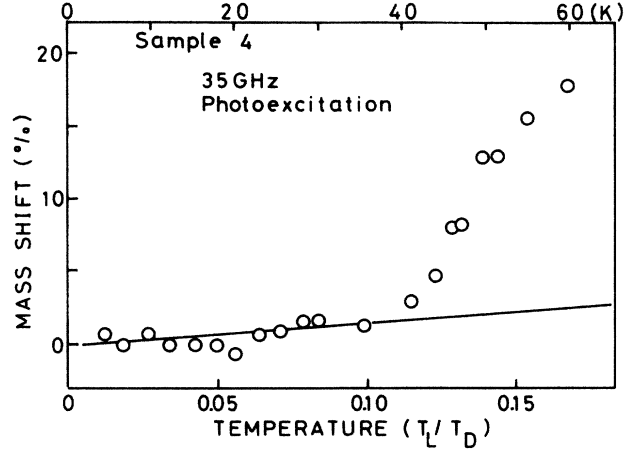

FIG. 14. Temperature dependence of the relative cyclotron mass shift $100[m^*(T_L) - m^*(4.2\text{ K})]/m^*(4.2\text{ K})$. The data are taken at a delay time of 4 μs and from sample 4. The temperature is scaled by the Debye temperature $T_D = 360$ K. The solid line shows a theoretical prediction by Eq. (17).

There are a few things other than the polaron effect which influence the resonance-peak position. At high temperatures or at high impurity concentration, a small $\omega\tau$ value pushes the peak position to low magnetic field. The correction due to this effect, however, is found to cause a reduction of only 2% at 60 K. The resonance position also shifts towards the low magnetic field by the polarization effect as the electron density is increased. The correction is again found to cause a reduction of only a few percent for the carrier density less than 10^{12} cm^{-3}. The band mass of electrons tends to decrease as the temperature is raised, on account of narrowing of the band gap. The apparent cyclotron mass, however, shows the opposite behavior.

Peeters and Devreese have made a calculation of the polaron mass based on the generalized Feynman polaron model.[28,29] They give

$$m_p^* = \left[1 + \frac{\alpha}{6}\left[1 + \frac{9}{4\beta}\right]\right]m_b^* \tag{17}$$

at the weak-coupling and low-temperature limits, i.e., $\alpha \ll 1$ and $\beta \gg 1$. Here, m_p^* is the polaron mass, m_b^* the band mass, and $\beta = T_D/T_L$, with $T_D = \hbar\omega_{LO}/k_B$. In Fig. 14 the experimental results for the polaron-mass shift are compared with the theoretical calculation by Peeters and Devreese. The material constants and T_D are the same as previous ones. We see from Fig. 14 that there is as large a discrepancy as a factor of 5 at $T_L/T_D \sim 0.15$ between theory and experiment, the experimental values being greater.

Baxter et al. have reported measurements of the cyclotron effective mass of AgBr as a function of temperature.[30] Their experimental result is in disagreement with the temperature dependence of the polaron mass as predicted by existing theories. They have interpreted the large mass shift as arising from a resonant electron-phonon interaction between a conduction electron and a

bound-impurity state mediated by a LA phonon. Final explanation, thus, should await further experiments with different crystals.

IV. DISCUSSIONS

A. Samples containing 2D and 3D electrons

1. Delay-time dependence

In order to understand the delay-time and temperature dependencies of cyclotron-resonance absorption for samples 3 and 5, we have considered the 3D electrons coexisting with the 2D electrons confined in potential wells of the twin-crystal boundary. A schematic picture for the potential of twin-crystal boundary is shown in Fig. 15 for samples 3 and 5. Electrons are divided into three classes according to their characters. The electrons designated as a and c are the 3D electrons populated in limpid area and the 2D electrons with low mobility stagnant in potential wells, respectively. The electrons designated b, on the other hand, are the 2D electrons with high mobility which are thermally excited above the mobility edge for sample 3, or populated beyond the mobility edge because of high electron density for sample 5.

Let us consider the following kinetic equations for understanding the experimental results through the time-resolved cyclotron resonance for sample 3. At an arbitrary delay time after photoexcitation, the density of the 3D electrons will be denoted $n_3(t)$ and that of the 2D electrons $n_2(t)$. The 3D electrons generated at the limpid area by a photopulse are either captured by impurities or flow into the well. Accordingly, the rate equations are expressed as

$$\frac{dn_3}{dt} = -\frac{n_3}{\tau_3} - \frac{n_3}{\tau_{32}} + \frac{n_2}{\tau_{23}} \tag{18}$$

and

$$\frac{dn_2}{dt} = -\frac{n_2}{\tau_2} - \frac{n_2}{\tau_{23}} + \frac{n_3}{\tau_{32}} , \tag{19}$$

where $1/\tau_3$ and $1/\tau_2$ are the capture rates of the 3D and 2D electrons, respectively. $1/\tau_{32}$ is the flow rate from 3D

to 2D regions and $1/\tau_{23}$ the reverse flow rate. τ_3 and τ_2, obtained from the experimental results, are 2.0 and 60 μs, respectively. The solid lines in Fig. 16 are drawn after the calculation with Eqs. (18) and (19), using $\tau_{32}=5$ μs and $\tau_{23}=3$ μs as the fitting parameters. These parameters should depend on the excitation conditions. In other words, these values may not be universal. Experimental behavior, however, is well described by this simple model.

2. Temperature dependence

The temperature dependence of the cyclotron-resonance absorption for sample 3 is understood as follows: As the temperature is raised, the densities of both a and b electrons increase, and the cyclotron-resonance absorption of 3D as well as 2D nature becomes observable. This is apparently the temperature-dependent 3D-2D transition.

As already shown in Fig. 11, the resonance-absorption behavior for sample 5 strongly depends on temperature. Figure 17 shows the dependence of the absorption intensity of the 3D electrons on the reciprocal temperature. As mentioned above, the absorption by the 3D electrons gradually increases as the temperature is raised. The 2D electron absorption, on the other hand, stays substantially constant. These phenomena suggest that the 3D electrons exist in thermal equilibrium with the 2D electrons in the potential well at higher temperature. In thermal equilibrium the density of the 3D electrons outside the potential well is given by

$$n_3(T) = 2 \left[\frac{m^* k_B T_L}{2\pi\hbar^2} \right]^{3/2} \exp\left[-\frac{\phi}{k_B T_L} \right] , \tag{20}$$

where ϕ is the energy difference between the conduction-band edge in the limpid area and the Fermi level E_F in the potential well. This is the so-called work function.
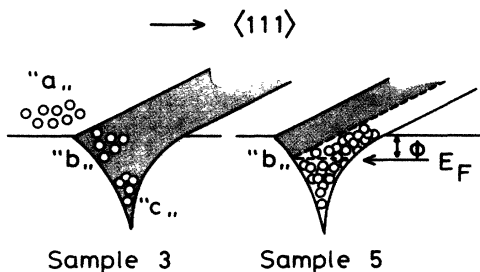
FIG. 15. A schematic picture for the potential well of a twin-crystal boundary for samples 3 and 5. Three kinds of electrons are designated a, b, and c. See text for their characteristics. The Fermi energy E_F and a work function ϕ for the degenerate 2D electrons in sample 5 are shown.
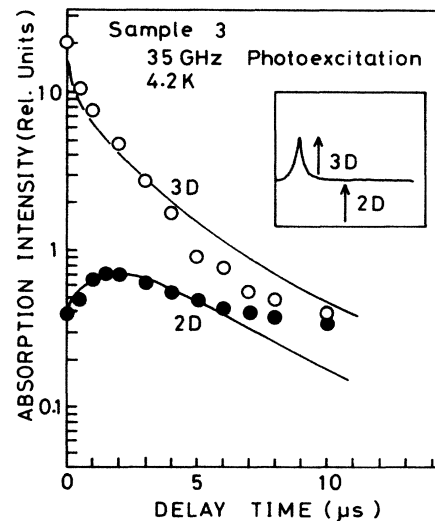
FIG. 16. Decay profiles of cyclotron-resonance absorption (3D) and nonresonant absorption (2D) after a photoexcitation pulse for sample 3. Two solid lines represent the calculations with our proper parameters according to Eqs. (18) and (19).
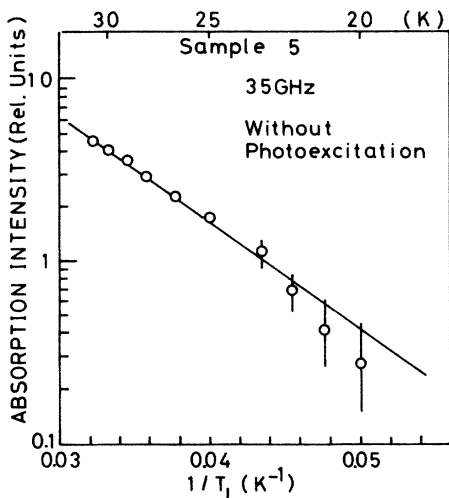
FIG. 17. Temperature dependence of the 3D electron-cyclotron-resonance absorption intensity plotted vs the reciprocal temperature for sample 5. The data are taken without photoexcitation. The solid straight line drawn through the data points yields the value of the work function $\phi = 8.9$ meV according to Eq. (20) (see text).
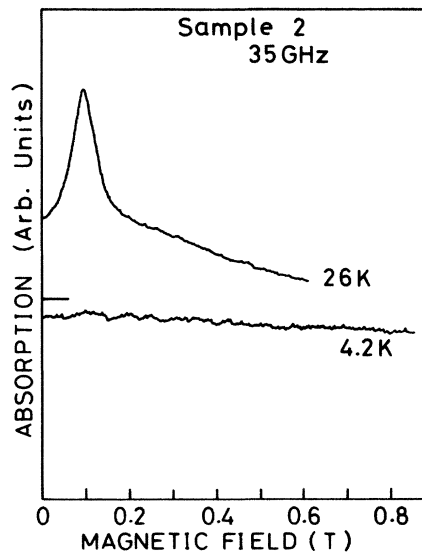

FIG. 18. Cyclotron-resonance traces, taken at 4.2 and 26 K right after the excitation pulse, from sample 2. At 4.2 K only a broad plateau is observed. The ground level for each trace is shifted.

The solid straight line drawn through data points in Fig. 17 yields the value of $\phi = 8.9$ meV according to Eq. (20).

B. Sample treated in selenium vapor

When the density of electrons is sufficiently low as in sample 2, the electrons can move around, at low temperatures, only in a limited region of the potential well with random spatial variation and hardly give rise to a well-defined resonance peak. As shown in Fig. 18, we have observed only a broad plateau at 4.2 K. At 26 K the electron cyclotron resonance exhibiting the normal bulk behavior is observed only right after the excitation pulse.

C. 2D-3D transition induced by magnetic field

In Fig. 4 we can see two resonance peaks at 4.2 K: a sharp peak at lower magnetic field and a relatively broad peak at higher magnetic field. While a sharp resonance peak is isotropic for various orientations of the magnetic field, the resonance field of a broad peak is sensitive to the magnetic field direction. The situation is analogous to experimental results at 20 K with microwaves for sample 5. In the case of the microwave experiment, however, only a single resonance line due to the 2D electrons is observed at 4.2 K, as shown in Fig. 10. A difference between the two experiments is the resonance field. This means that even at 4.2 K a part of the 2D electrons behaves like the 3D electrons under a high magnetic field.

The dimensionality of electrons in a 2D attractive potential well and their transport properties are determined by the relative size of the "characteristic length" of electrons to the width of the potential. In a strong magnetic field the characteristic length corresponds to the cyclotron radius of electrons. When the cyclotron radius becomes smaller than the well width, electronic behavior is

no longer two dimensional and the transport properties of the system change their characters. A part of the 2D electrons, which are populated in the higher-energy level of the well, turn into the 3D electrons induced by the magnetic field. In other words, when $\hbar\omega_c$ is much greater than the intersubband spacings, cyclotron transitions between the $N = 0$ and 1 Landau levels of many subbands coexist, which is the 3D limit. The above arguments, such as for the dimensionality of electrons, are consistent with our previous experimental results for thin metallic films.[31] Detailed quantitative discussions would be worth making in a future extended study.

V. CONCLUSIONS

Various new features of electronic properties in ZnSe have been observed by far-infrared laser, as well as by millimeter wave, cyclotron resonance. The two-dimensional nature of electrons localized at the twin-crystal boundaries has been emphasized. The x-ray analysis and subsequent microscopic observation with polarizers support the model, suggested by the systematic cyclotron resonance, of a 2D attractive potential associated with an array of twin-crystal boundaries.

We have measured the temperature dependence of the electron-scattering rate through the linewidth measurement of the cyclotron resonance. The linewidth seems to consist of two effects, i.e., electron-phonon and electron–neutral-impurity interactions.

We obtain the work function for the coexisting system of the 3D and 2D electrons through the temperature dependence of the relative intensity of two cyclotron-resonance signals.

Furthermore, it is found that the polaron effect is essential for understanding the far-infrared experimental result, or the appearance of the second resonance peak,

and the temperature-dependent mass shift in the millimeter wave experiment.

ACKNOWLEDGMENTS

[1] F. Mandel, Phys. Rev. 134, A1073 (1964).
[2] G. F. Neumark, J. Appl. Phys. 51, 3383 (1980).
[3] K. M. Lee, Le Si Dad, and G. D. Watkins, Solid State Commun. 35, 527 (1980).
[4] P. J. Dean and J. L. Merz, Phys. Rev. 178, 1310 (1969).
[5] T. Taguchi and T. Yao, J. Appl. Phys. 56, 3002 (1984).
[6] M. Isshiki, T. Yoshida, K. Igaki, W. Uchida, and S. Suto, J. Cryst. Growth 72, 162 (1985).
[7] T. Steiner and M. L. W. Thewalt, Solid State Commun. 56, 933 (1985).
[8] M. Aven and B. Segall, Phys. Rev. 130, 81 (1963).
[9] T. Yao, M. Ogura, S. Matsuoka, and T. Morishita, Appl. Phys. Lett. 43, 499 (1983).
[10] E. Otsuka, Jpn. J. Appl. Phys. 25, 303 (1986).
[11] T. Ohyama, H. Kobori, and E. Otsuka, Jpn. J. Appl. Phys. 25, 1518 (1986).
[12] T. Ohyama, K. Fujii, and E. Otsuka, Jpn. J. Appl. Phys. 21, 865 (1982).
[13] T. Ohyama, Phys. Rev. B 23, 5445 (1981).
[14] T. Ohyama, E. Otsuka, T. Yoshida, M. Isshiki, and K. Igaki, Jpn. J. Appl. Phys. 23, L382 (1984).
[15] T. Ohyama, E. Otsuka, T. Yoshida, M. Isshiki, and K. Igaki, Surf. Sci. 170, 491 (1986).
[16] T. Ohyama, K. Sakakibara, E. Otsuka, M. Isshiki, and K. Masumoto, Jpn. J. Appl. Phys. 26, L136 (1987).
[17] E. Otsuka, T. Ohyama, H. Nakata, and Y. Okada, J. Opt. Soc. Am. 67, 931 (1977).
[18] D. M. Larsen, in Polarons in Ionic Crystals and Polar Semiconductors, edited by J. T. Devreese (North-Holland, Amsterdam, 1972), Chap. III.
[19] K. K. Bajaj, Phys. Rev. 170, 694 (1968).
[20] F. M. Peeters and F. T. Devreese, Phys. Rev. B 31, 3689 (1985).
[21] D. L. Rode, Phys. Rev. B 2, 4036 (1970).
[22] M. Aven, D. T. F. Marple, and B. Segall, J. Appl. Phys. 32, 2261 (1961).
[23] C. Erginsoy, Phys. Rev. 79, 1913 (1950).
[24] B. Ray, II-VI Compounds (Pergamon, Oxford, 1969).
[25] J. Bardeen and W. Schockley, Phys. Rev. 80, 72 (1950).
[26] H. J. G. Meyer and D. Polder, Physica 19, 255 (1961).
[27] G. D. Mahan, in Polarons in Ionic Crystals and Polar Semiconductors, Ref. 18, Chap. VI.
[28] F. M. Peeters and J. T. Devreese, Phys. Rev. B 31, 5500 (1985).
[29] F. M. Peeters and J. T. Devreese, Physica B + C 127B, 408 (1984).
[30] J. E. Baxter, G. Ascarelli, and S. Rodriguez, Phys. Rev. Lett. 27, 100 (1971).
[31] T. Ohyama, M. Okamoto, and E. Otsuka, J. Phys. Soc. Jpn. 54, 1041 (1985).

Sample 3

$\langle 1\,1\,1 \rangle \longrightarrow$

Sample 5

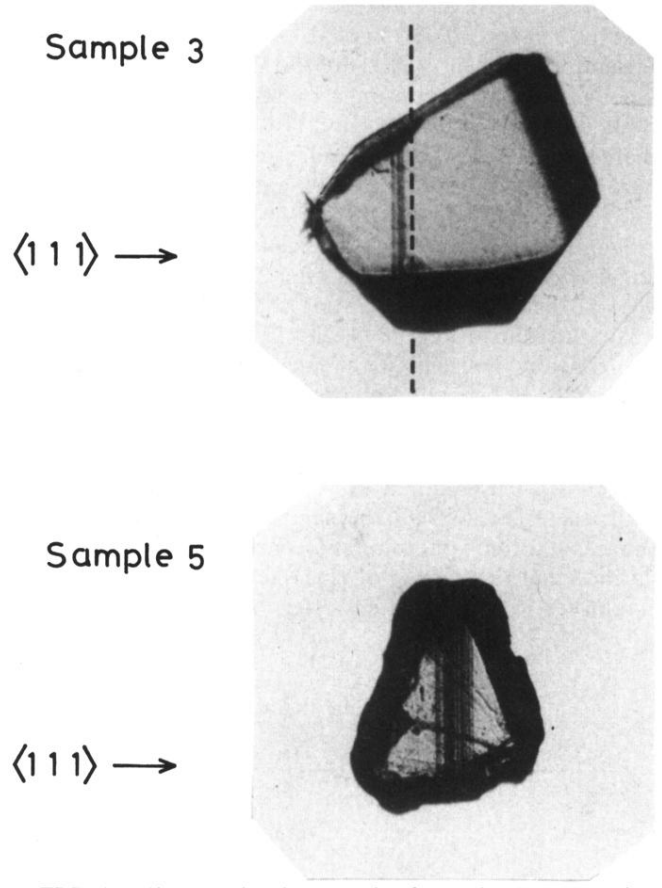$\langle 1\,1\,1 \rangle \longrightarrow$

FIG. 1. Microscopic photograph of samples 3 and 5 taken with a couple of optical polarizers. Distinct multimosaic structures are visible in both samples. Arrows show the relevant crystallographic axes. The dashed line parallel to "stripes" shows a cutting line. The larger part without "stripes" is designated as sample 4.
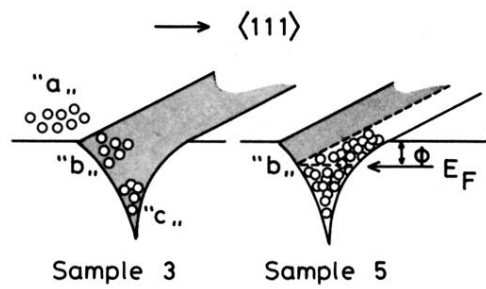
FIG. 15. A schematic picture for the potential well of a twin-crystal boundary for samples 3 and 5. Three kinds of electrons are designated a, b, and c. See text for their characteristics. The Fermi energy E_F and a work function ϕ for the degenerate 2D electrons in sample 5 are shown.